

# Experimental and Computational Flow Field Studies of a MAV-scale Cycloidal Rotor in Forward Flight

Tejaswi Jarugumilli<sup>1</sup>

Andrew H. Lind<sup>2</sup>

Moble Benedict<sup>3</sup>

Vinod K. Lakshminarayan<sup>4</sup>

*Alfred Gessow Rotorcraft Center,  
University of Maryland, College Park, MD*

*Dept. of Aeronautics and Astronautics  
Stanford University, CA*

Anya R. Jones<sup>5</sup>

Inderjit Chopra<sup>6</sup>

*Alfred Gessow Rotorcraft Center, University of Maryland, College Park, MD*

## ABSTRACT

This paper provides a fundamental examination of the flow physics for a two-bladed MAV-scale cycloidal rotor (or cyclorotor) in forward flight using experimental particle image velocimetry (PIV) measurements, computational studies (2D CFD) and time-averaged performance measurements. A simple aerodynamic analysis using time-averaged flow field measurements from PIV is used to develop a basic understanding of the distribution of blade aerodynamic forces and power along the rotor azimuth. The incoming flow velocity is shown to decrease in magnitude as the flow passes through the upper half of the rotor. This is attributed to power extraction by the blades in the upper-frontal region of the rotor azimuth. Flow field measurements also show a significant increase in flow velocity across the lower half of the rotor cage. The aerodynamic analysis demonstrates that the blades accelerate the flow through the lower-aft region of the rotor, where they operate in a high dynamic pressure environment with a large positive effective angle of attack. CFD-predicted values of instantaneous aerodynamic forces reveal that the aft section of the rotor is the primary region of force production. Phase-averaged flow field measurements are also analyzed. These results reveal two blade wakes in the flow, formed by each of the two blades. Analysis of the blades at several azimuthal positions revealed two significant blade-wake interactions in the aft of the cyclorotor. The locations of these blade-wake interactions are correlated with force peaks in the CFD-predicted instantaneous blade forces, implying that unsteady aerodynamic interactions play an important role in the lift and propulsive force generation of the cyclorotor.

## NOTATION

$b$	Blade span	$\theta$	Pitch angle
$c$	Blade chord length	$\theta_A$	Half peak-to-peak pitch amplitude
$D$	Rotor diameter	$\mu$	Advance ratio
$N_b$	Number of blades	$\Phi$	Rotor phase angle
$U_\infty$	Freestream velocity	$\Omega$	Rotor rpm
$X, Y, Z$	Rotor coordinate system	$\Psi$	Blade azimuthal position
$u$	Horizontal component of velocity		
$v$	Vertical component of velocity		
$\alpha$	Angle of attack		
$\alpha_i$	Virtual incidence angle		

## INTRODUCTION

In response to the increasing need for smaller unmanned aerial vehicles (UAVs) and rapid advancements in miniaturized electronic systems during the past decade, a new class of flying machines called micro air vehicles (MAVs) has emerged. The ultimate design goals for MAVs include a gross takeoff weight of less than 100 g and maximum length dimensions less than 15 cm (Ref. 1). The potential for MAVs to perform a wide range of missions in cost-effective and low-risk ways could make them powerful assets in both military and civilian applications in the future.

Presented at the 69<sup>th</sup> Annual Forum, Phoenix, Arizona, May 21-23, 2013. Copyright © 2013 by the authors. Published by the AHS International with permission. All Rights reserved.

<sup>1</sup> Graduate Research Assistant. [jtsn423@umd.edu](mailto:jtsn423@umd.edu)

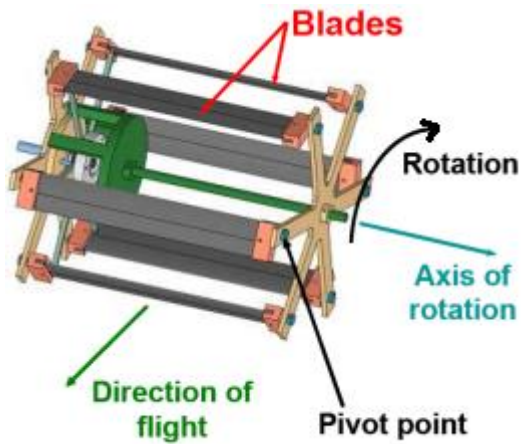
<sup>2</sup> Graduate Research Assistant. [alind@umd.edu](mailto:alind@umd.edu)

<sup>3</sup> Assistant Research Scientist. [moble@umd.edu](mailto:moble@umd.edu)

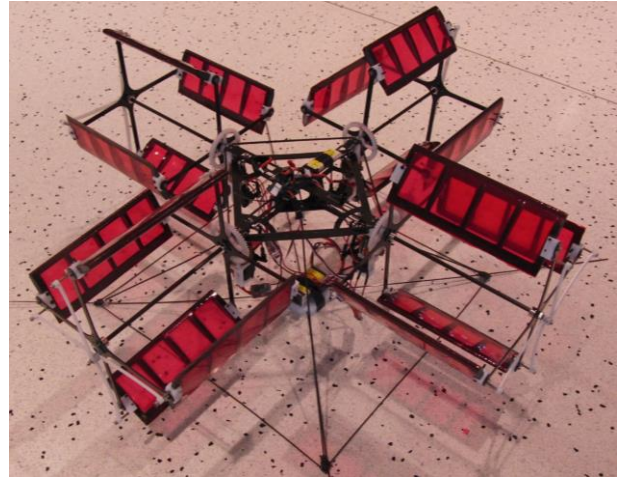
<sup>4</sup> Postdoctoral Fellow. [vinodkl@stanford.edu](mailto:vinodkl@stanford.edu)

<sup>5</sup> Assistant Professor. [arjones@umd.edu](mailto:arjones@umd.edu)

<sup>6</sup> Alfred Gessow Professor and Director. [chopra@umd.edu](mailto:chopra@umd.edu)



(a) Cycloidal rotor.



(b) Cycloidal-rotor based MAV capable of autonomous hover developed at the University of Maryland.

**Figure 1. Cycloidal rotor system.**

Some examples of potential missions include surveillance and reconnaissance in the battlefield, biochemical sensing, traffic monitoring, fire and rescue operations, border surveillance, wildlife surveys, power line inspection and real estate aerial photography.

Currently, the prevailing choice for a hover-capable MAV utilizes a conventional edge-wise rotor. However, MAVs operate in a low Reynolds number flight regime where a conventional rotor faces severely degraded aerodynamic performance (Ref. 2). Recently, a cycloidal-rotor (cyclorotor) based MAV has been proposed as a potential alternative (Fig. 1) (Ref. 3). The cyclorotor consists of a set of blades that follow a circular trajectory about a horizontal axis of rotation (Fig. 1(a)). A passive four-bar pitching mechanism allows each blade to achieve positive pitch angles in both halves of its circular trajectory (Fig. 2). These pitching kinematics allow the rotor to produce a net non-zero aerodynamic force. The magnitude and direction of the net force vector can be controlled by varying the amplitude and phasing of the blade pitching kinematics.

The advantages of a cycloidal rotor system stem from its potential for higher aerodynamic efficiency, increased maneuverability and high-speed forward flight. Unlike a conventional helicopter rotor, where aerodynamic conditions vary significantly along the blade span, all span-wise blade elements of the cyclorotor operate under similar conditions (i.e. similar flow velocities, Reynolds numbers, and angles of incidence). The relatively uniform distribution of forces along the blade span allows the cyclorotor to be more easily optimized for maximum aerodynamic efficiency. Previous experimental studies have shown that a cyclorotor can achieve a higher aerodynamic

power loading (thrust/power) in hover compared to a conventional rotor of similar scale (Ref. 3). A second advantage of a cyclorotor is its thrust vectoring capability. The net thrust vector can be instantaneously set to any direction perpendicular to the axis of rotation by introducing a phasing in the pitching kinematics. Thus, the cyclorotor concept may provide relatively better maneuverability compared to a conventional rotor based MAV, making it ideal for operations in highly confined and gusty environments. Furthermore, previous studies have shown several advantages of the cyclorotor in forward flight (Refs. 4-5), two of which include the achievement of high forward flight speeds (up to 13 m/s) with significant reductions in power consumption and the ability to transition from hover to forward flight without significant changes to vehicle attitude or configuration.

The cycloidal rotor concept has been explored for aviation applications since the early 20<sup>th</sup> century (Refs. 6-9). However, experimental data and analytical models for rotor performance are scarce, especially at MAV-scales. Most previous experiments were conducted at relatively large scales ( $Re > 100,000$ ) and primarily restricted to the hover condition (Refs. 6-12). A detailed background on many of these earlier studies is presented in Ref. 13.

The present work is a continuation of previous efforts at the University of Maryland aimed to understand the forward flight performance of a MAV-scale cyclorotor (Refs. 4-5). Previous studies primarily involved time-averaged experimental performance measurements of the rotor lift, propulsive force and power at different advance ratios and varying blade pitching kinematics (i.e. blade pitch amplitude, pitch phase angle and symmetry of pitching).

The current work utilizes time-resolved, planar particle image velocimetry (PIV) techniques to gain a fundamental understanding of the flow environment. This is the first known study which employs experimental techniques to examine the flow field of a cyclorotor in forward flight. In addition to the PIV studies, computational studies (2D CFD) and time-averaged experimental performance measurements were conducted. The key contributions of the CFD studies in this work are predictions of the instantaneous blade forces and power along the rotor azimuth. In general, it is difficult to implement devices (e.g. pressure taps, strain gages) to experimentally measure instantaneous blade forces on MAV-scale rotary wing systems due to the imposed space constraints and high centrifugal load environments in which they operate. Therefore, the CFD studies are integral to this work as they provide instantaneous aerodynamic blade loads.

The goal of the current work is to develop a fundamental understanding of the governing flow physics and how it affects the force production on a cyclorotor in forward flight. In turn, the findings in this study may aid in the design and development of an efficient, high-speed flight capable cyclocopter MAV.

The remaining sections of the paper are organized as follows. First, the definitions and rotor coordinate system for the cyclorotor are introduced. Next, the experimental setup and procedures for the PIV studies and performance measurements are discussed, followed by the methodology and validation for the 2D CFD studies. Flow field results are presented and correlated with experimental and computational aerodynamic forces. Lastly, the key conclusions from this study are summarized.

## DEFINITIONS AND ROTOR COORDINATE SYSTEM

The coordinate system for the cyclorotor used in the present study is shown in Fig. 2. The rotor operates in the clockwise direction, with the freestream velocity flowing from left to right. The azimuthal position of each blade,  $\Psi$ , is measured in the clockwise direction originating from the positive Y-axis. The blade pitch angle,  $\theta$ , is the angle formed by the blade chord line and the tangent to the circular trajectory of the blade. The blade pitching kinematics are represented as a sinusoidal function:

$$\theta(\Psi) = \theta_A \sin(\Psi + \Phi)$$

Here,  $\theta_A$  is half the total peak-to-peak pitch amplitude and  $\Phi$  is the pitch phase angle. For all the cases considered in this work, the phase angle is maintained at  $\Phi=90^\circ$ . This corresponds to the blades achieving maximum pitch angles

at azimuthal locations of  $\Psi=0^\circ$  (rotor front) and  $\Psi=180^\circ$  (rotor rear/aft). This is illustrated in Fig. 2. In addition, the peak-to-peak pitch amplitude is maintained constant at  $70^\circ$  (i.e.  $\theta_A=35^\circ$ ) for all cases.

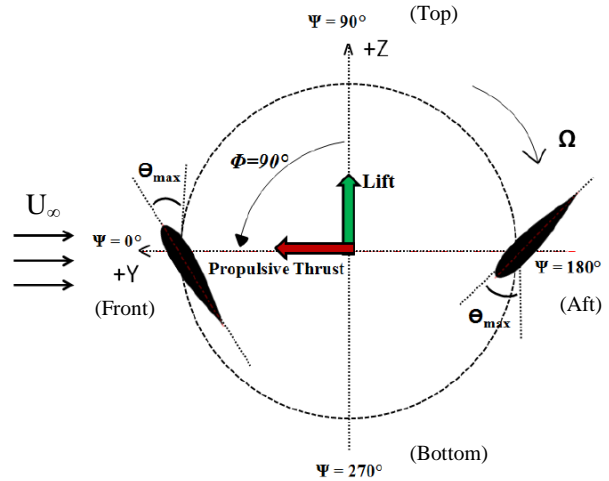


**Figure 2. Rotor coordinate system (forward flight).**

This study examined rotor performance at different advance ratios ( $\mu$ ), the ratio of freestream flow velocity to the blade tip speed:

$$\mu = \frac{U_\infty}{\Omega R}$$

The rotor lift force is defined as the net aerodynamic force produced in the +Z-direction (perpendicular to the freestream) and the propulsive thrust is the net aerodynamic force in the +Y-direction (Fig. 2). The total aerodynamic power includes the induced power, profile power and rotational flow losses associated with the blades. The power associated with the rotation of the blade support structure (e.g. endplates, linkages, etc.) was removed from the power measurements to isolate the aerodynamic power of the blades.

## EXPERIMENTAL SETUP AND PROCEDURES

In the current work, flow field measurements were obtained using time-resolved, planar (two-component) particle image velocimetry (PIV). Time-averaged performance measurements were acquired using a custom-built force balance system. The experimental work is compared with a computational fluid dynamics (CFD) analysis. The current section describes each setup in detail as well as the validation techniques for the CFD analysis.

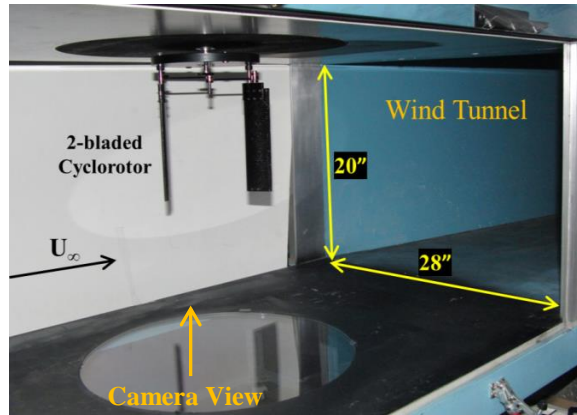


Figure 3. PIV experimental setup.

Table 1. Characteristics of the experimental cyclorotor.

Parameter	Measurement
Number of blades ( $N_b$ )	2
Blade span ( $b$ )	6.25 in
Blade chord length ( $c$ )	1.95 in
Rotor radius ( $R$ )	3 in
Airfoil section	NACA 0015

#### Particle Image Velocimetry (PIV) Experimental Setup

A two-bladed cyclorotor was designed and built specifically for the PIV experiments, as shown in Fig. 3. Two blades were chosen as it is the simplest model of a cyclorotor. Although increasing the number of blades introduces additional aerodynamic interactions, the general operating principles of the rotor are unaffected. The dimensions of the cyclorotor used in these experiments are presented in Table 1. The PIV experiments were conducted in a low-speed, open-circuit/closed-section wind tunnel with test section dimensions of 20 x 28 in and maximum speed of 100 mph. The flow was seeded with vaporized mineral oil at the inlet of the wind tunnel. A double-pulsed high-speed laser illuminated the seeding particles (Litron LDY304 Nd:YLF laser, 30 mJ/pulse at 1 kHz rep-rate). The laser sheet was positioned at the mid-span of the rotor to minimize the presence of three-dimensional tip effects. A square 8 in mirror was used to redirect a portion of the laser sheet back toward the rotor to reduce the shadows cast by the blades. A high-speed camera (Phantom V311, 1MPx, 3,250 fps) was positioned below the test section and oriented upward to view the blades through a circular acrylic window (the camera view angle is shown in Fig. 3). The rotor was mounted vertically in the test section with the blades cantilevered. The blade pitching mechanism was located at the root, permitting an unobstructed field of view for the camera. PIV experiments were conducted with the rotor at 1200 rpm (blade speed of 9.58 m/s) for three different freestream velocities of  $U_\infty=3, 5$  and 7 m/s; these cases correspond to advance ratios of  $\mu=0.31, 0.52$  and 0.63.

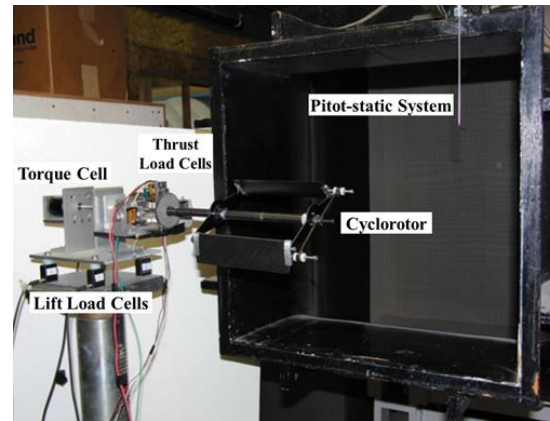


Figure 4. Open-jet wind tunnel experimental setup.

Freestream velocities were determined using PIV measurements of the mean flow in the test section (without the rotor present).

**PIV Processing:** Image pairs were acquired at a sampling rate of 1.6 kHz. The rotor operated at 1200 rpm (20 Hz), resulting in data sets with measurements at 80 rotor azimuthal positions per rotor revolution (azimuthal resolution of 4.5°). All PIV acquisition and processing was performed using DaVis v8.1.3 by LaVision. Raw images were preprocessed using a spatial background subtraction filter to increase the signal-to-noise ratio (image contrast). Regions where the velocity field was undefined (i.e. blades, shadows and areas of low seeding) were excluded (i.e. masked) from processing. The maximum particle displacement between the two frames of each image pair was approximately 4-7 pixels. A multi-pass cross-correlation algorithm was performed with one pass of a 64 x 64 pixel window and two passes of a 32 x 32 pixel window; each pass implemented a 50% window overlap. Circular windows were used to eliminate the bias effects encountered along the diagonals of traditional square windows. The resulting spatial vector field provided a grid of 81 x 51 vectors (in the Y x Z directions). Spurious vectors accounted for less than 5% of the total vector field and were replaced with second-, third-, or fourth-choice vectors using a remove-and-replace median filter. This was only applied to spurious vectors whose variance from the median of eight neighboring vectors was more than twice the variance of these neighboring vectors.

#### Open-Jet Wind Tunnel Setup

In addition to PIV flow field measurements, time-averaged performance measurements were conducted on the two-bladed cyclorotor. The experimental setup is shown in Fig. 4. These experiments were performed using a low speed, open-circuit/open section wind tunnel with outlet dimensions of 22 x 22 in. Although the cyclorotor dimensions remained the same as in the PIV studies, the

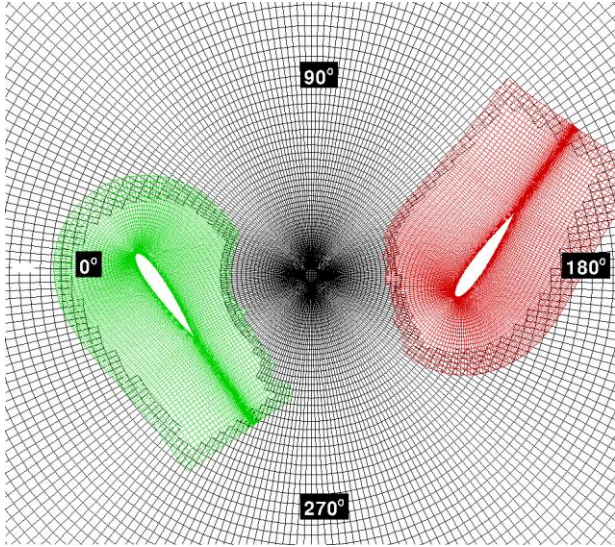


Figure 5. 2-D CFD mesh grid.

boundary conditions at the rotor tip were different, as the blades were not cantilevered. An endplate was added to the free-end of the rotor to prevent excessive vibrations, which otherwise affected the force measurements. A 3-component force balance (Fig. 4) was used to measure rotor lift, propulsive thrust and shaft torque. A Hall-effect sensor measured the rotational speed of the rotor, which in turn was used to calculate the total aerodynamic power. For each test case, tare runs were performed without the blades and these measurements were subtracted from the total measurements.

Time-averaged force measurements were collected at 1200 rpm for freestream velocities of  $U_\infty=3, 5$  and  $7$  m/s, to correlate with the PIV studies. The freestream velocity was measured using a pitot-static system. An rpm sweep was also performed from 600 to 1400 rpm (in increments of 200 rpm) with a constant freestream velocity of 3 m/s. This served as a baseline case for CFD validation. For each case, individual test runs were performed six times to ensure sufficient repeatability; these measurements were averaged to obtain the final results presented in this paper. It is important to note that the two-bladed cyclorotor operated near system resonance at a rotational speed of 800 rpm ( $\mu=0.47$ ). This prevented measurement of lift at 800 rpm, but it was still possible to obtain propulsive thrust and power measurements. Lastly, the ambient temperature and pressure were recorded prior to each experiment, and the corresponding density corrections were made to the measurements.

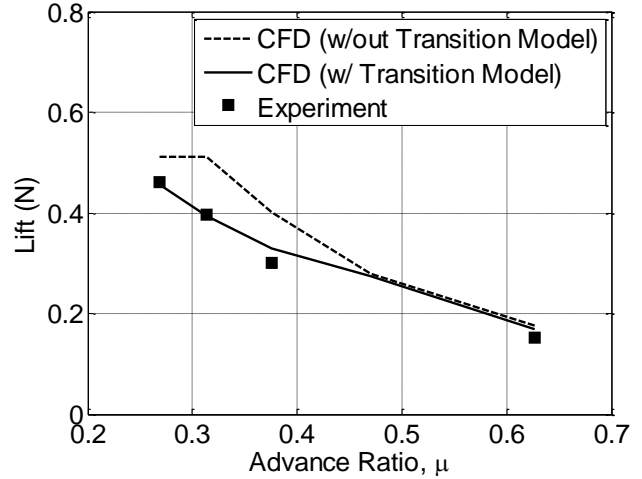


Figure 6. Comparison of time-averaged lift versus advance ratio between CFD and experiment.

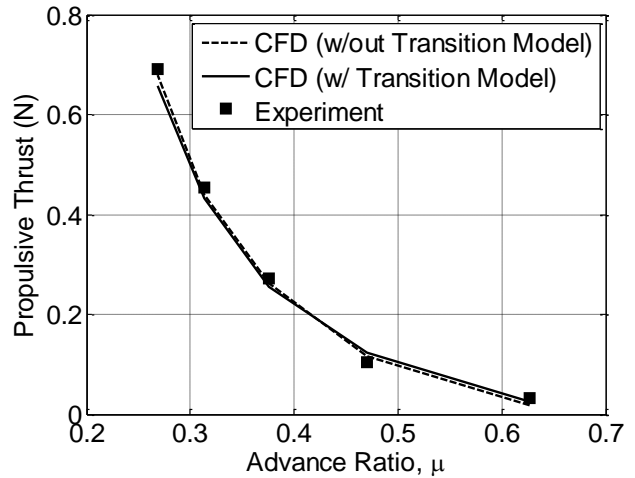


Figure 7. Comparison of time-averaged propulsive thrust versus advance ratio between CFD and experiment.

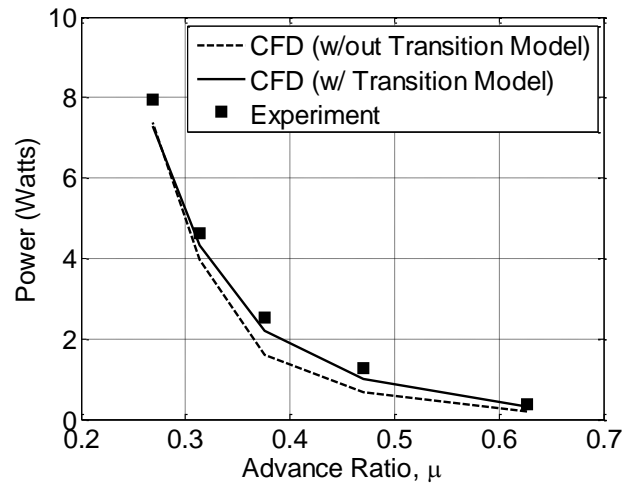


Figure 8. Comparison of time-averaged power versus advance ratio between CFD and experiment

## CFD METHODOLOGY AND VALIDATION

A 2-D CFD study was also conducted to understand the flow physics of the cyclorotor. The details of the flow solver and grid system used are discussed below.

**Flow Solver:** 2-D simulations of the cycloidal rotor were undertaken using a compressible structured overset RANS solver, OVERTURNS (Ref. 14). This overset structured mesh solver uses the diagonal form of the implicit approximate factorization method developed by Pulliam and Chaussee (Ref. 15) with a preconditioned dual-time scheme to solve the compressible RANS equations. Computations are performed in the inertial frame in a time-accurate manner. A third-order MUSCL scheme (Ref. 16) with Roe flux difference splitting (Ref. 17) and Koren’s limiter (Ref. 18) is used to compute the inviscid terms, and second-order central differencing is used for the viscous terms. Due to the relatively low operating Mach numbers of the present cyclorotor, the inclusion of a low Mach preconditioner based on Turkel’s (Ref. 19) method accelerates the convergence and ensures accuracy of the solution. Spalart-Allmaras (SA) (Ref. 20) turbulence model is employed for RANS closure. This one-equation model has the advantages of ease of implementation, computational efficiency and numerical stability. Furthermore, because of the transitional nature of the flow-field, the CFD simulations were performed with and without the use of a transition model. A two equation  $\gamma - \overline{Re}_{\theta t}$  - SA model of Medida and Baeder (Ref. 22) is employed in the simulations using the transition model.

**Grid System:** An overset system of meshes, consisting of C-type airfoil mesh for each blade and a cylindrical background mesh is used for the computation. The airfoil meshes have 255 x 55 grid points in the wraparound and normal directions, respectively. The background cylindrical

mesh has 245 x 221 points in the azimuthal and radial directions, respectively. An implicit hole-cutting method developed by Lee (Ref. 21) and refined by Lakshminarayan (Ref. 14) is used to find the connectivity information between the overset meshes. Figure 5 shows the mesh system. In this figure, only the field points (points where the flow equations are solved) are shown. All the points that are blanked out either receive no information from another mesh or lie inside a solid body and therefore do not have a valid solution.

### CFD vs. Experiment: Time-Averaged Force Comparison

Prior to utilizing the instantaneous force data predicted by CFD, the time-averaged lift, propulsive thrust and power were validated with the experimental measurements. Figures 6-8 show a comparison between the CFD predictions and experimentally measured values for time-averaged aerodynamic forces and power. The CFD-predicted values show strong correlation with the experimental measurements, both with and without the transition model. However, the CFD results with the transition model show better correlation with experiment; therefore, all CFD results presented in the following sections include the transition model. Even though the use of a transition model improves the prediction, the results without a transition model also showed a good qualitative agreement and such simulations might still be valuable if a CFD code is not equipped with a transition model.

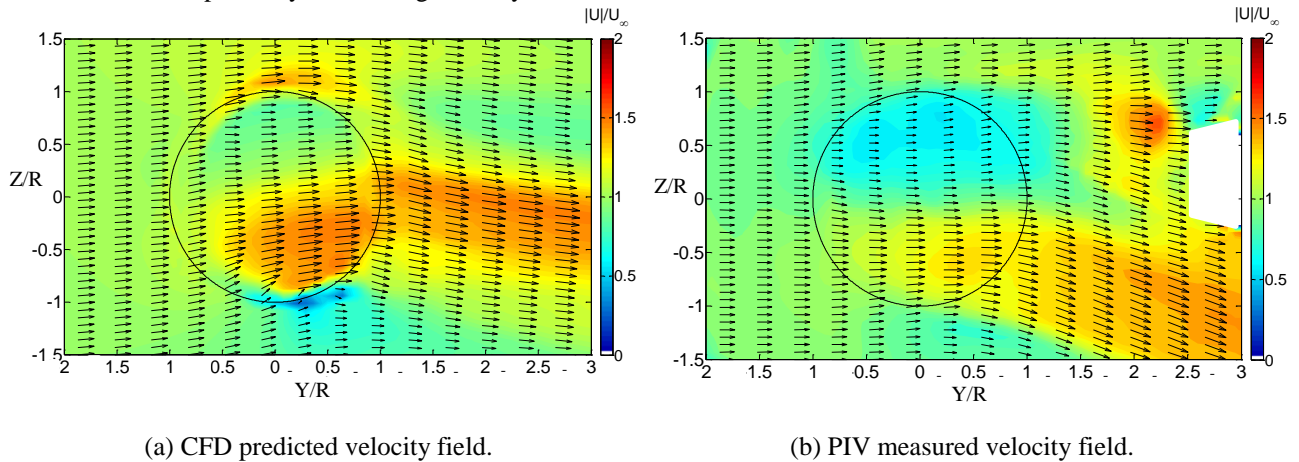


**Figure 9. Comparison of the time-averaged flow fields predicted by CFD and measured using PIV for an advance ratio of  $\mu=0.52$ .**

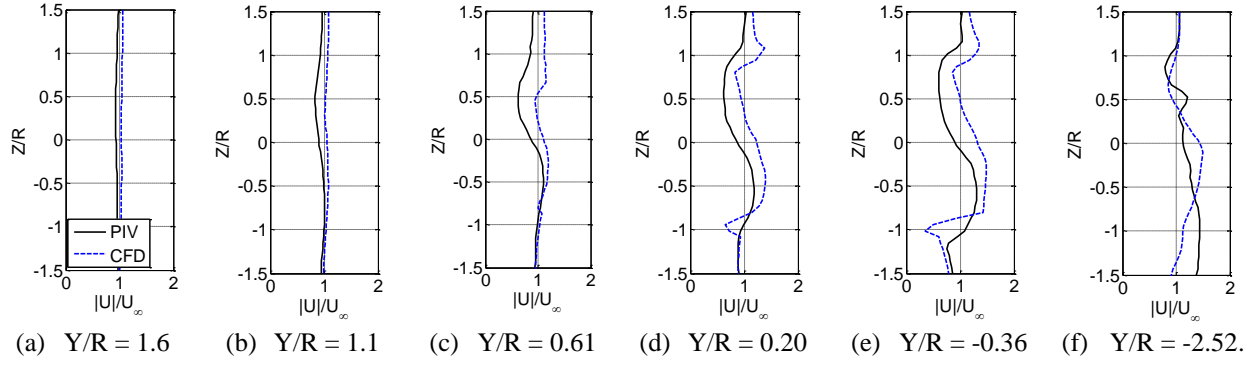


**Figure 10. Velocity profile distribution along Z/R direction at various Y/R locations for advance ratio  $\mu=0.52$ .**

### CFD vs. PIV: Flow Field Comparison

The flow field predicted by CFD was also compared to PIV measurements. The CFD solution was interpolated onto the PIV grid for the purpose of comparison. Figure 9 shows both the CFD predicted flow field and PIV measured flow field at an advance ratio of 0.52 ( $U_\infty=5\text{m/s}$ ,  $\Omega R=9.58\text{m/s}$ ). Although the purpose here is not to analyze the flow field characteristics, it can be seen that many of the flow features seen in the PIV measured flow field are captured in the CFD-predicted results. In both figures, a low velocity region exists in the upper half of the rotor cage while a high velocity region extends from the lower half of the rotor cage into the wake. Figure 10 shows normalized velocity profiles of the time-averaged flow field along the Z-direction at various Y/R locations (i.e. vertical sectional cuts). A comparison between CFD and PIV is made using these velocity profiles. In general, CFD over-predicts the magnitude of the velocity profile, but the general trends are reflected by the CFD analysis. Overall, these comparisons between CFD predictions and experimental measurements provide sufficient confidence in the CFD results.

## RESULTS AND DISCUSSION

### Time-Averaged PIV Flow Field

The objective of the current section is to examine the mean (or time-averaged) flow field of the cyclorotor and develop a basic understanding of the distribution of aerodynamic forces along the rotor azimuth. A simple aerodynamic analysis based on PIV flow field measurements will be used in conjunction with the CFD-predicted instantaneous forces and power to fulfill this objective.

The time-averaged flow field for the cyclorotor was determined by averaging instantaneous velocity field measurements acquired through PIV. The instantaneous velocity fields were averaged over one complete rotor revolution (80 images per revolution) and these results were

subsequently averaged for multiple rotor revolutions. A total of 10 rotor revolutions (800 images) were averaged for advance ratio  $\mu=0.52$  and 5 rotor revolutions (400 images) for advance ratios  $\mu=0.31$  and  $\mu=0.73$ . Masked regions were excluded from the averaging process.

The time-averaged flow fields corresponding to the three advance ratios are shown in Figs. 11-13. In these images, each vector represents the local flow velocity and its magnitude was calculated using the horizontal ( $u$ ) and vertical ( $v$ ) velocity components:

$$|U| = \sqrt{u^2 + v^2}$$

The velocity field is normalized by the freestream flow, which travels from left to right. Also, the Y and Z distances have been non-dimensionalized by the rotor radius (R), with the rotation axis of the cyclorotor located at (Y/R, Z/R) = (0, 0).

Several key insights can be gained from Figs. 11-13. First, for all three advance ratios, it can be seen that the flow velocity decreases in magnitude as it passes through the upper half of the rotor cage (the area enclosed by the circular blade path). For example, in Fig. 11, the local flow velocity at point A is  $|U|_A=2.4\text{m/s}$  which is 20% lower than the freestream value of  $U_\infty=3\text{m/s}$ . These results can be more clearly seen for the higher advance ratio cases of  $\mu=0.52$  and  $\mu=0.73$  (Figs. 12 and 13), where the flow velocity at point A is nearly 30% lower than the freestream value in each case. The decreased magnitude of the flow velocities in this region suggests that the blades are extracting energy between azimuthal positions of  $\Psi=0^\circ$  to  $\Psi=90^\circ$ .

Figures 11-13 also show that the flow gains momentum as it approaches and passes through the lower-rear quadrant of the rotor ( $\Psi=180^\circ$  to  $\Psi=270^\circ$ ). At point B in Fig. 11, the flow velocity is nearly 80% greater ( $|U|_B=5.4\text{m/s}$ ) than the freestream value. The flow in the upper half also gains momentum as it exits the upper-rear quadrant of the rotor ( $\Psi=90^\circ$  to  $\Psi=180^\circ$ ), as seen by the increased flow velocities

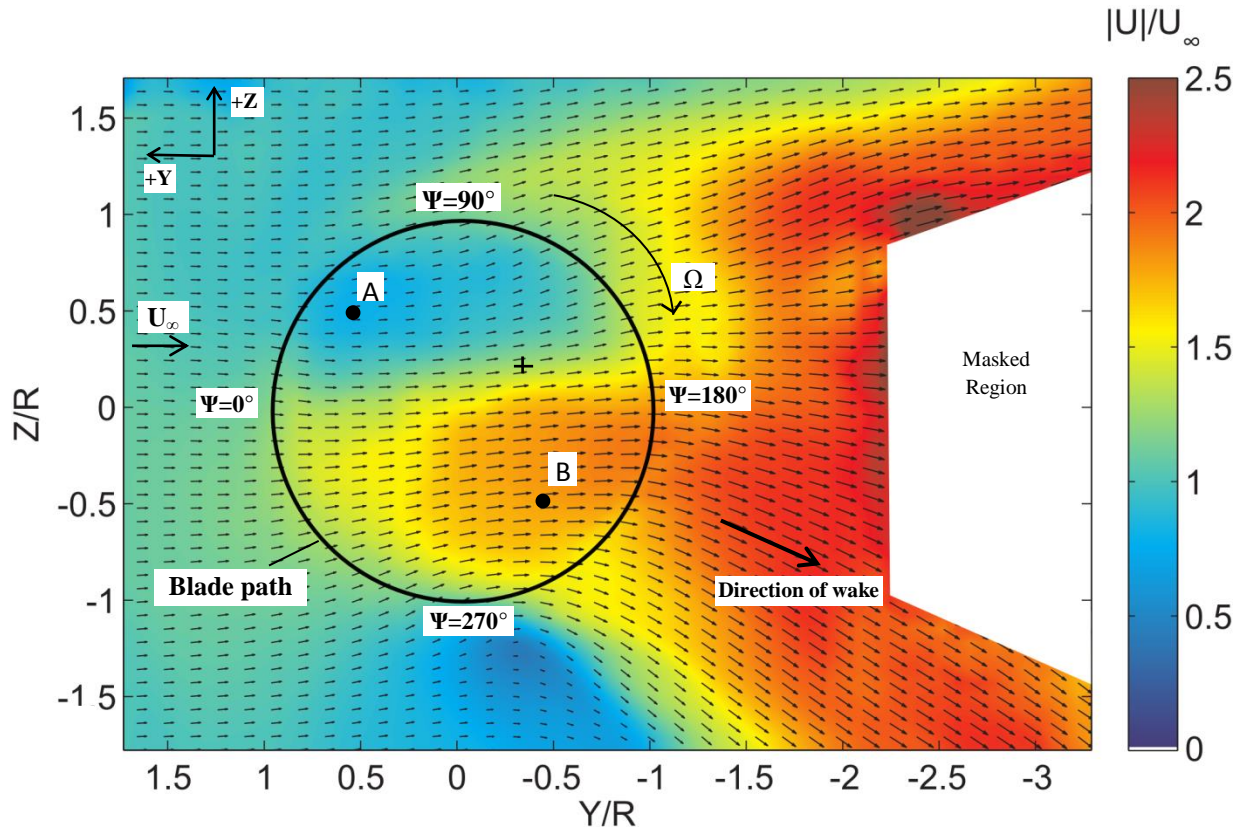


Figure 11. Time-averaged velocity field calculated using PIV measurements at advance ratio  $\mu=0.31$  ( $U_\infty=3$  m/s,  $\Omega R=9.58$  m/s).

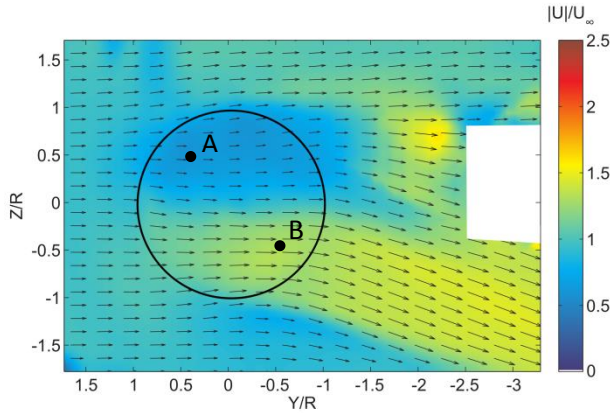


Figure 12. Time-averaged velocity field calculated using PIV measurements at advance ratio  $\mu=0.52$  ( $U_\infty=5$  m/s,  $\Omega R=9.58$  m/s).

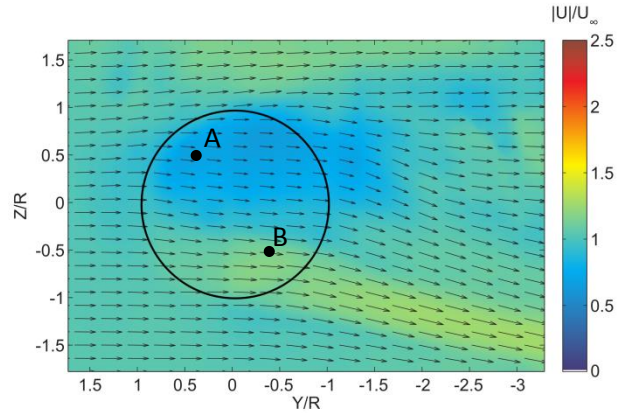


Figure 13. Time-averaged velocity field calculated using PIV measurements at advance ratio  $\mu=0.73$  ( $U_\infty=7$  m/s,  $\Omega R=9.58$  m/s).

Table 2. Experimentally measured time-averaged rotor lift, propulsive force, and power for three advance ratios.

Advance Ratio ( $\mu$ )	Lift (N)	Propulsive Force (N)	Power (W)
0.31	0.40	0.45	4.63
0.52	0.49	0.26	3.55
0.73	0.64	0.06	2.50

in the rotor wake. These observations imply that the blades are adding energy to the flow in the rear half of the cyclorotor. This is especially true in the lower-rear quadrant ( $\Psi=180^\circ$  to  $\Psi=270^\circ$ ), where the most significant increases in local flow velocities are visible.

The net increase in momentum in the  $-Y$ -direction suggests that the rotor is producing a positive net propulsive force. Furthermore, the downward change in direction of the flow in the rotor wake (Fig. 11(a)) corresponds to a net momentum change in the  $Z$ -direction, which implies the rotor is producing a net lift force. Together, these observations for rotor lift and propulsive force are confirmed by time-averaged performance measurements presented in Table 2. For all three advance ratios, the rotor produces positive lift and propulsive force. It is also evident from Table 2 that the rotor power decreases with increasing advance ratio; this is likely due to increased power extraction by the blades between  $\Psi=0^\circ$  to  $\Psi=90^\circ$ .

Using CFD, it is possible to obtain predictions of the instantaneous lift, propulsive force and power distributions along the rotor azimuth. These results are presented in Figs. 14-16. From Fig. 14, it is interesting to note that the majority of the positive lift force is produced in the lower-rear quadrant of the rotor ( $\Psi=180^\circ$  to  $\Psi=270^\circ$ ), for all three advance ratios. Also, the blade produces a slightly negative lift in most of the upper half ( $\Psi=45^\circ$  to  $\Psi=135^\circ$ ). Figure 15 reveals that the rear half of the rotor ( $\Psi=90^\circ$  and  $\Psi=270^\circ$ ) is the primary propulsive force producing region. The blades generally produce a negative propulsive force across the frontal half ( $\Psi=270$  to  $\Psi=90^\circ$ ) which increases in magnitude with advance ratio (Fig. 15). Lastly, Fig. 16 shows the variation of power along the rotor azimuth. It is interesting to note that the blades experience negative values of power (i.e. power extraction) along the frontal half of the rotor, especially in the upper-frontal quadrant ( $\Psi=0^\circ$  to  $\Psi=90^\circ$ ). These negative values of power are consistent with the decreased flow velocities observed in this region previously in the time-averaged PIV flow field.

At this point, a simple aerodynamic analysis will be presented to help develop a better understanding of the results just presented in Figs. 11-16. Specifically, the local aerodynamic environment of the blade will be examined at eight different azimuthal positions. The observations made in this analysis will then be used to explain the distribution of the rotor lift, propulsive force and power along the rotor azimuth. The analysis will be carried out for a moderate advance ratio of  $\mu=0.52$ .

At any given azimuthal position, the three key factors that determine whether the local blade forces contribute to the rotor lift or propulsive force are: 1) the magnitude of the local resultant velocity acting on the blade, 2) the effective aerodynamic angle of attack of the blade and 3) the

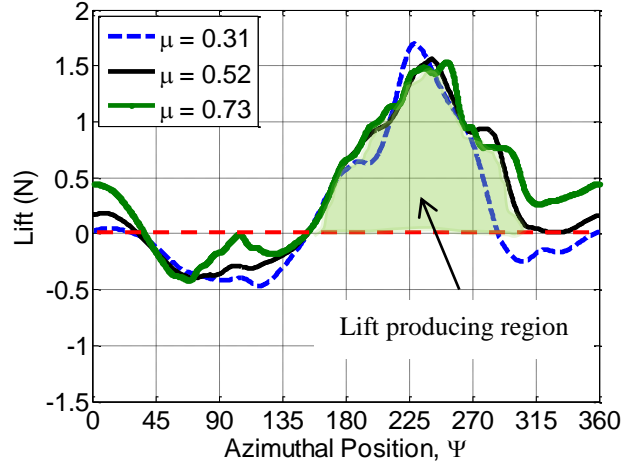


Figure 14. CFD-predicted instantaneous blade lift vs. azimuth for different advance ratios.

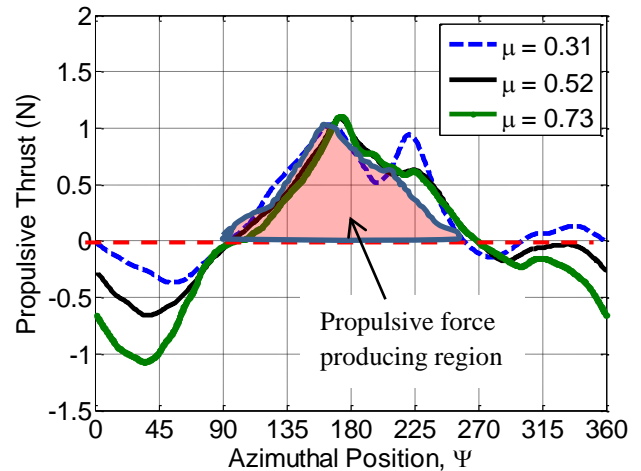


Figure 15. CFD-predicted instantaneous blade propulsive force vs. azimuth for different advance ratios.

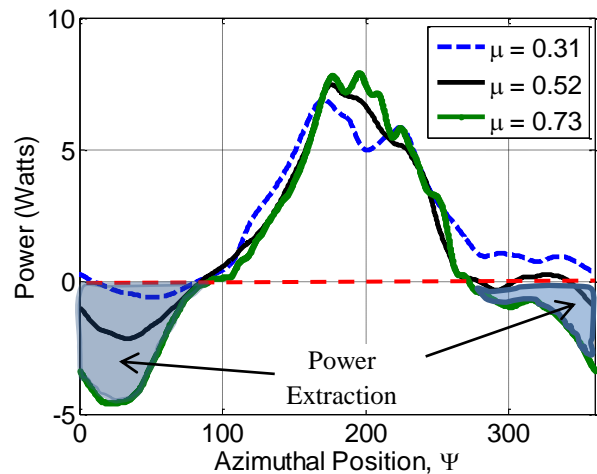
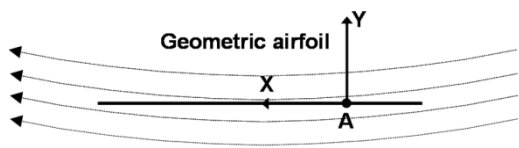
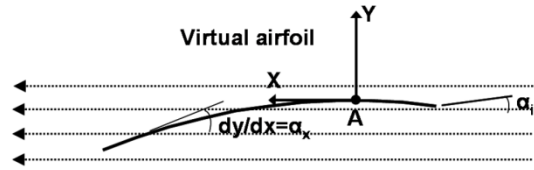


Figure 16. CFD-predicted instantaneous blade power vs. azimuth for different advance ratios.

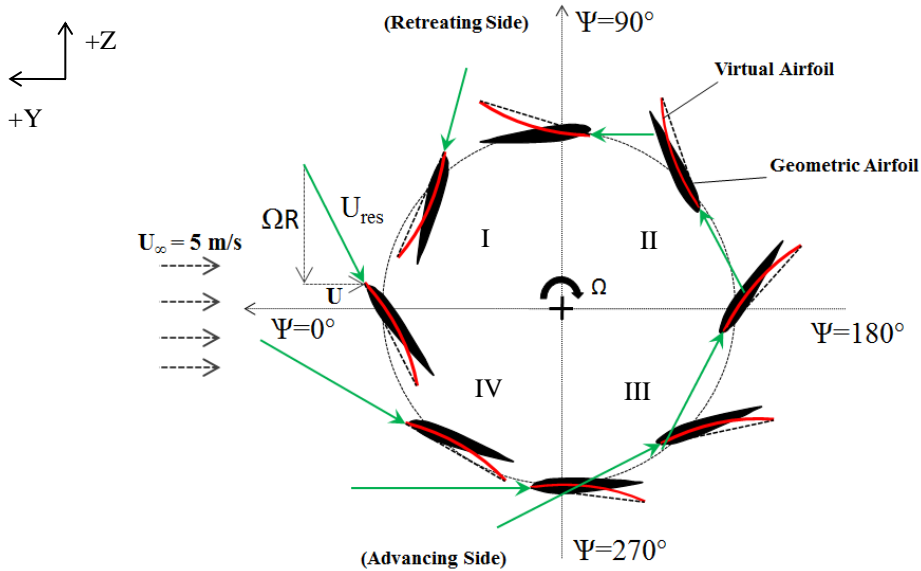


(a) Geometric airfoil in curvilinear flow.

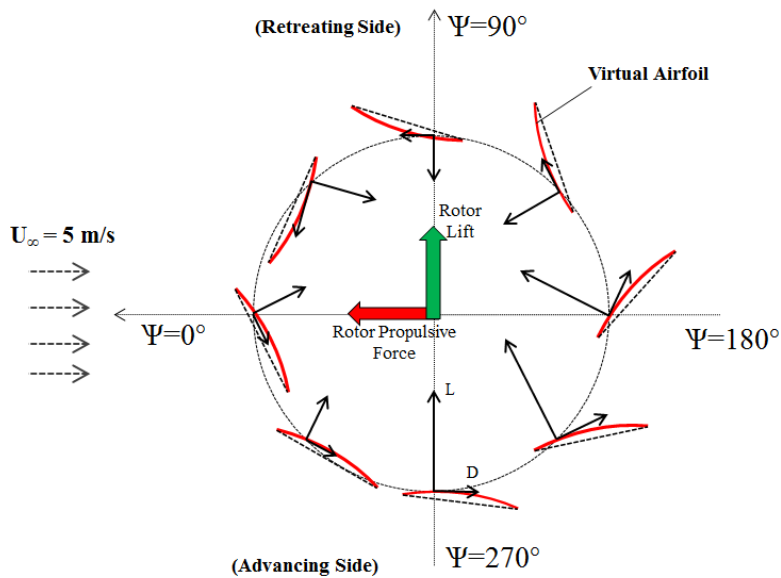


(b) Virtual airfoil with camber and incidence in rectilinear flow.

**Figure 17. Schematic illustrating flow curvature effects on a cyclorotor.**



(a) Geometric and virtual airfoils with local resultant velocity vectors.



(b) Lift and drag forces on the blade.

**Figure 18. Schematics showing local aerodynamics of blade at several azimuthal positions for advance ratio  $\mu=0.52$ .**

orientation of the blade with respect to the freestream. The magnitude and direction of the local resultant velocity vector with respect to the blade chord line can be obtained through a vector summation of the local flow velocity and the blade tangential velocity:

$$\vec{U}_{resultant} = \vec{U}_{local} + \vec{U}_{blade}$$

For simplicity, the local flow vector will be assumed to be in the direction of the freestream. The magnitude of the local flow velocities at various azimuthal positions are obtained using the mean flow field results from PIV.

The effective aerodynamic angle of attack of the blade is a function of the geometric pitch angle ( $\theta$ ), the angle of attack between the resultant velocity vector and the blade chord line ( $\alpha$ ), as well as an incidence angle ( $\alpha_i$ ) which results from flow curvature effects on the blade:

$$\alpha_{eff} = f(\theta, \alpha, \alpha_i)$$

Flow curvature effects on the blades of a cyclorotor result from a chordwise variation of the local blade velocity, which can be attributed to the orbital motion of the blades (Ref. 23). These effects are discussed in detail in Ref. 4. For the scope of this paper, it is sufficient to consider that these flow curvature effects are due to a curvilinear flow along the blade chord. Furthermore, a geometrically symmetric airfoil immersed in a curvilinear flow can be represented as a cambered airfoil in a rectilinear flow. This is illustrated in Fig. 17. For the cyclorotor used in the present study ( $R=3$  in,  $c=1.95$  in,  $c/R=0.65$ ), a linear approximation (Ref. 23) shows that the virtual camber is approximately 8% of the blade chord. In addition, due to the fact that the blade pitching axis is positioned at the quarter-chord and not at the mid-chord, the blade experiences a virtual incidence angle, which is approximately  $9^\circ$  (calculated using the linear model in Ref. 23). Therefore, these values for camber and incidence clearly suggest that flow curvature effects are not negligible for the present cyclorotor. In order to account for flow curvature effects in the current aerodynamic analysis, the *geometric* airfoil is represented as a *virtual* airfoil that features both camber and incidence angle.

The schematics presented in Fig. 18 are derived using the aerodynamic analysis discussed above. Figure 18(a) shows the blade at the eight different azimuthal positions previously listed. Here, the camber line (red) corresponds to the *virtual* airfoil and is superimposed on the *geometric* airfoil. The local resultant velocity vectors acting on the blade at each azimuthal position are also sketched (in green). Note that these velocity vectors are drawn to scale, based on the local flow velocity ( $U$ ) and the blade tangential velocity ( $\Omega R$ ). The local flow velocities ( $U$ ) were obtained using the PIV measured mean flow, as described

earlier in this section. Using the information provided in Fig. 18(a), the directions of the local blade lift and drag forces can be obtained and are shown in Fig. 18(b). Together, the schematics in Fig. 18 will now be used to explain the contributions of the local blade forces to the overall rotor lift and propulsive force in various regions of the rotor azimuth.

**Region I ( $\Psi=0^\circ$  to  $\Psi=90^\circ$ ):** At  $\Psi=0^\circ$ , the effective angle of attack of the blade is approximately zero, as depicted in Fig. 18(a). However, the blade is still expected to produce a lift force due to its virtual camber. Based on the orientation of the blade with respect to the freestream, the blade lift force is expected to increase the net rotor lift, but decrease the net propulsive force (Fig. 18(b)). The CFD-predicted results in Figs. 14-15 support this finding, as they show negative values for propulsive force and positive values for lift.

At  $\Psi=45^\circ$ , the blade operates with a slightly positive effective angle of attack. However, the orientation of the blade is such that the lift force acts to decrease both rotor propulsive force and rotor lift. Furthermore, the blade produces a force in the direction opposing the freestream flow and as a result the incoming flow velocity is expected to decrease across this region. This is consistent with the observations made previously in the PIV flow field measurements (Figs. 12). In reducing the flow velocities, the blade extracts energy from the flow; this is evidenced by the negative values of power observed in the CFD results (Fig. 16).

**Region II ( $\Psi=90^\circ$  to  $\Psi=180^\circ$ ):** At  $\Psi=90^\circ$ , the blade operates with an increased effective angle of attack. However, it is clear from Fig. 18(b) that the orientation of the blade is such the majority of the blade lift force will be in the  $Z$ -axis direction, which in turn decreases the net rotor lift. This coincides with the negative values of lift observed in this region from CFD predicted results (Fig. 14). It should be noted, however, that the blade is in the retreating half of the rotor in this region and therefore experiences lower local resultant velocities. Thus, the decreases in net rotor lift will be less pronounced.

At  $\Psi=135^\circ$ , the blade is at a slight positive effective angle of attack. Based on the orientation of the blade in Fig. 18(b), the local lift force has components in the  $+Y$ -direction and  $-Z$ -direction. Therefore, the blade increases the net rotor propulsive force, but continues to decrease the net rotor lift. It should be recalled that the local flow velocities in this region are lower in magnitude due to the power extraction by the blades in region I. Therefore, the blade effective angle of attack in region II will be slightly greater compared to region I.

**Region III ( $\Psi=180^\circ$  to  $\Psi=270^\circ$ ):** At  $\Psi=180^\circ$ , the blade has an increased effective angle of attack. The orientation

of the blade reveals that the blade contributes to both the net rotor lift and propulsive force. It can be seen that the contribution of the blade forces to the rotor propulsive force will be maximum at an azimuthal location between  $\Psi=135^\circ$  and  $\Psi=180^\circ$ , when its local lift vector becomes parallel to the free stream. This observation is captured in the CFD-predicted results in Fig. 15, where the maximum propulsive force value occurs at approximately  $\Psi=170^\circ$ .

At  $\Psi=225^\circ$ , the blade experiences a large positive effective angle of attack (Fig. 18(a)). Therefore, as shown in Fig. 18(b), the local aerodynamic forces on the blade are significant. Furthermore, the orientation of the blade suggests blade lift force will have components in the  $+Y$ - and  $+Z$ -directions. Thus, the blade contributes to rotor propulsive force and lift in this region.

**Region IV ( $\Psi=270^\circ$  to  $\Psi=0^\circ$ ):** At  $\Psi=270^\circ$ , the blade is still at a relatively large positive effective angle of attack. Fig. 18(b) shows that the majority of the blade lift force is along the  $+Z$ -direction and therefore the primary contribution will be to the rotor lift.

At  $\Psi=315^\circ$ , the blade is close to a zero effective angle of attack. However the virtual camber allows the blade to produce a non-zero local lift force, which has components in the  $-Y$ - and  $+Z$ -directions. Thus, the blade still contributes to the net rotor lift, but decreases the net propulsive force in this region.

### Effect of Advance Ratio

Although the above aerodynamic analysis was carried out for one particular advance ratio ( $\mu=0.52$ ), the same general principles were found to hold true for the lower and higher advance ratios ( $\mu=0.31$  and  $\mu=0.73$ ) considered in this study. However, the effective angle of attack distribution of the blades along the rotor azimuth will be different due to variations in the freestream velocity (constant  $\Omega$ ). From the CFD results presented in Figs. 14-16, it can be seen that the primary lift and propulsive force producing regions remain relatively the same for the three different advance ratios. Figure 16 shows that the effect of increasing advance ratio is to increase the power extraction along the frontal half of the rotor ( $\Psi=270^\circ$  to  $\Psi=90^\circ$ ), whereas the power in the rear half of the rotor azimuth remains relatively constant. This is a key reason for the decrease in power observed in the time-averaged experimental measurements (Table 2).

The analysis just presented uses a simplified model, but it effectively provides a fundamental understanding of the physics behind the distribution of forces and power along the rotor azimuth. These insights can assist with the design of a rotor for a flight-capable cyclocopter MAV. For example, asymmetric pitching kinematics, where one-half

of the rotor operates at a higher pitch angle than the corresponding half, may help improve rotor propulsive efficiency by leading to a more uniform azimuthal distribution of forces (Ref. 24). Also, the idea of using geometrically cambered airfoils for improving cyclocopter performance may be worthwhile to consider.

### Phase-Averaged PIV

Time-averaged PIV results provide insight into the mean flow field of a cyclocopter, but do not show the effects of unsteady aerodynamic flow features. The current section uses phase-averaged PIV measurements to quantify unsteady flow features and evaluate their impact on the aerodynamic performance of the blades at specific azimuthal positions.

As previously described, flow field measurements with high temporal resolution were acquired using a time-resolved PIV system. The sampling rate was 1.6 kHz and the rotor operated at 20 Hz. This provided flow field measurements at 80 azimuthal positions per rotor revolution (in  $4.5^\circ$  increments). Of these 80 azimuthal positions, four pairs are presented in this paper. Azimuthal positions can be paired due to the symmetry of the two-bladed rotor, with the blades denoted as blade A and blade B. For example, when blade A is positioned at  $\Psi_A=0^\circ$ , blade B is positioned at  $\Psi_B=180^\circ$ , etc. Instantaneous flow field measurements for each pair of azimuthal positions were isolated from the data set. The data set spanned 9.5 full rotor revolutions; images were extracted for each rotor half-revolution (due to rotor symmetry) giving 19 instantaneous flow field measurements for each pair of azimuthal positions. These measurements consist of two velocity components (in the  $Y$ - and  $Z$ -directions). The instantaneous velocity components for the 19 images at a single azimuthal position were then averaged. Phase-averaging in this way highlights prominent periodic flow features and reduces the appearance of aperiodic effects in the flow.

In the following analysis, phase-averaged results will be considered for the moderate advance ratio case of  $\mu=0.52$  ( $U_\infty=5$  m/s,  $\Omega=1200$ rpm). Emphasis is placed on the rear half of the rotor azimuth, where the blades operate in the wake of the frontal half and are therefore exposed to several unsteady aerodynamic flow features (most notably, blade-wake interactions).

### Flow Periodicity

Phase-averaging highlights the periodic features of a flow. Flow periodicity can be assessed by comparing the variance of a vertical velocity profile located at the center of the rotor cage ( $Y/R = 0$ ) for multiple rotor revolutions. Figure 19(a) shows profiles of total velocity (normalized by the freestream velocity) for the 19 instantaneous flow field

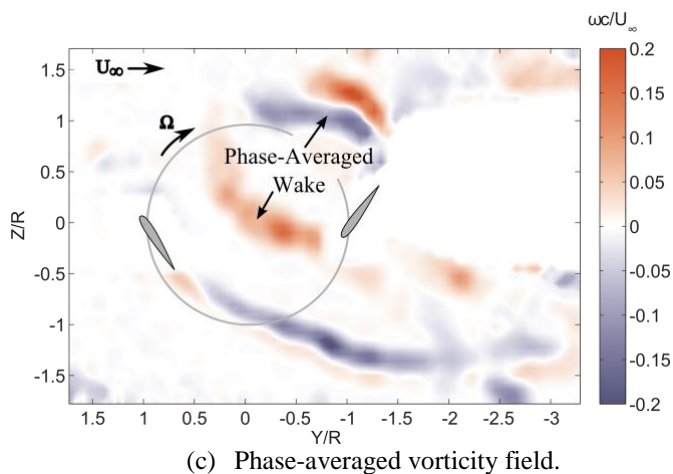
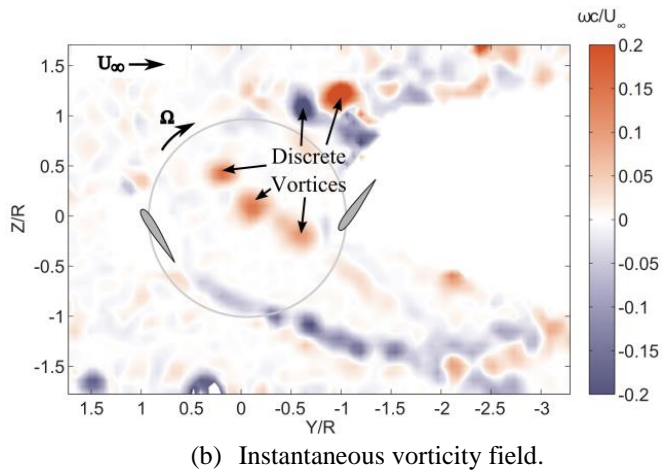
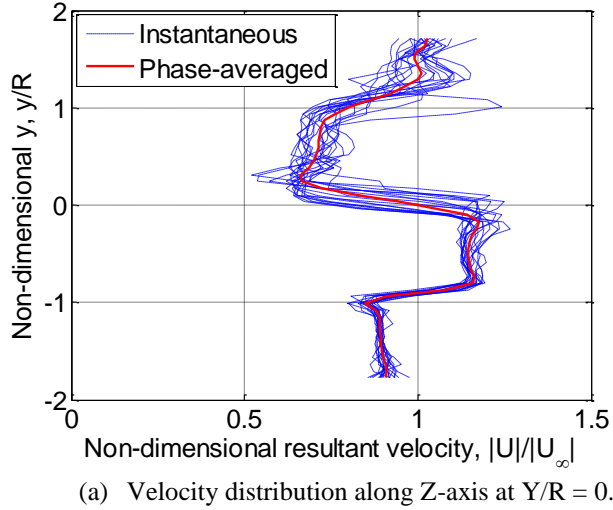


**Figure 19. Comparison of instantaneous and phase-averaged flow with blades at  $\Psi_A=0^\circ$  and  $\Psi_B=180^\circ$  ( $\mu=0.52$ ).**

images (blue) as well as the final phase-averaged result (red). For the data shown here, the blades are at azimuthal locations of  $\Psi=0^\circ$  (rotor forward) and  $\Psi=180^\circ$  (rotor aft). In general, the instantaneous velocity profiles show good agreement; the aperiodicity of the flow is captured in the deviations of the instantaneous velocity profiles from the phase-averaged velocity profile. The effects of phase-averaging on the flow field are illustrated in Fig. 19(b-c) where an instantaneous vorticity field is compared with the phase-averaged vorticity field. The instantaneous vorticity field (Fig. 19(b)) reveals numerous discrete vortices, especially in the upper-rear quadrant ( $\Psi=90^\circ$  to  $\Psi=180^\circ$ ) of the rotor. The phase-averaged vorticity field (Fig. 19(c)) appears more diffuse, which can be attributed to variations in the spatial position and intensity of the vortices between rotor revolutions. However, it can be seen that the phase-averaged vorticity field more clearly shows the general shape and trajectory of the blade wakes. A detailed discussion on these blade wakes follows in the remainder of this section.

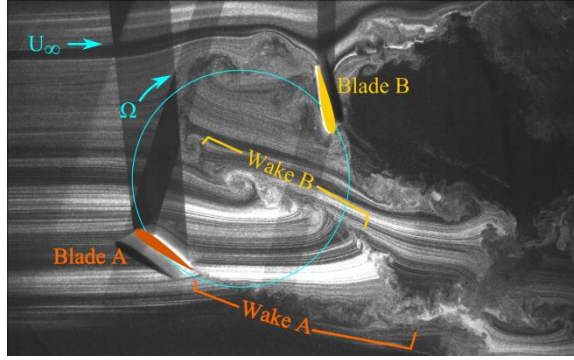
### Blade-Wake Interactions

Figs. 20-23 show phase-averaged flow fields for different blade azimuthal positions. Each figure consists of: (a) an instantaneous smoke flow visualization image, (b) the total velocity field, non-dimensionalized by the freestream velocity, and (c) the vorticity field, scaled by the blade chord and non-dimensionalized by the freestream velocity:

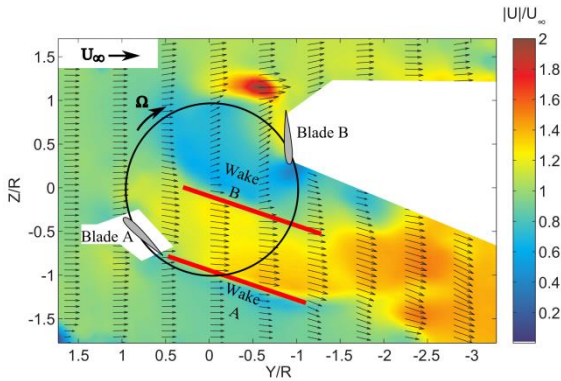
$$\omega^* = \frac{\omega c}{U_\infty}$$

In the velocity contour plots, only one-eighth of the total vectors calculated in the y-direction are shown for clarity. In the vorticity contour plots, positive vorticity (red) corresponds to counter-clockwise rotation and negative vorticity (blue) corresponds to clockwise rotation. In all figures, the freestream velocity is from left to right.

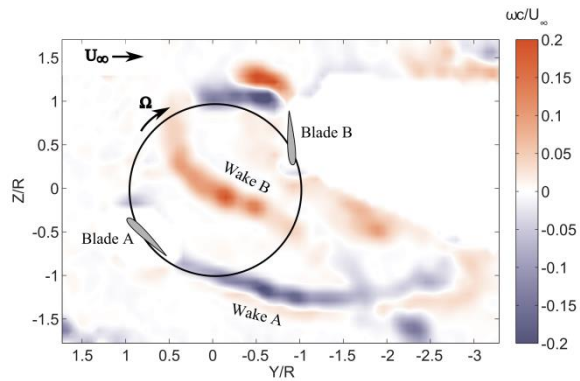
Figure 20 shows phase-averaged results for the two blades at azimuthal positions of  $\Psi_A=330^\circ$  and  $\Psi_B=150^\circ$ . The flow visualization image (Fig. 20(a)) reveals two wake structures (denoted as wakes A and B) generated by the blades. Wake A follows blade A, which experiences fully attached flow due to its low effective aerodynamic angle of attack in this region. Wake B follows blade B and has begun to convect downstream as a result of the incoming flow; the wake age of wake B is one-half of a rotor revolution older than wake A. The velocity contour plot in Fig. 20(b) illustrates the two shear layers formed by the blade wakes. The vorticity contour plot (Fig. 20(c)) reveals that wake A primarily consists of clockwise (negative) vorticity while wake B consists of a trail of counter-clockwise (positive) vorticity that extends through the rotor cage. A close look at the flow visualization reveals that these trails of vorticity are made



(a) Instantaneous flow visualization.

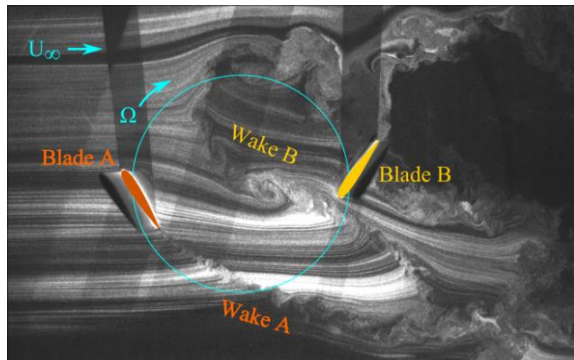


(b) Velocity field.

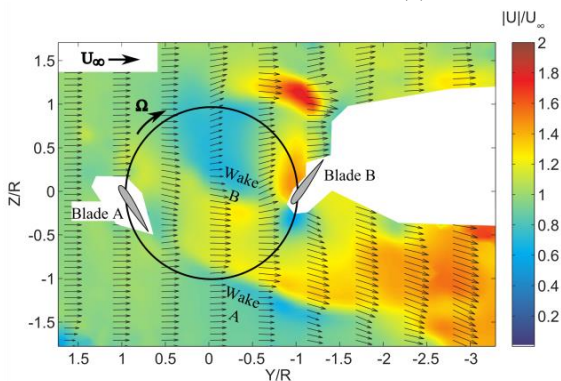


(c) Vorticity field.

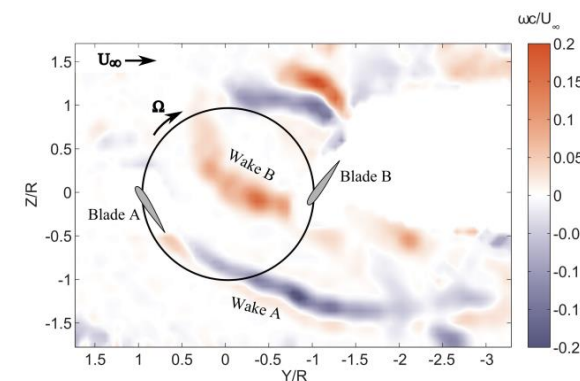
**Figure 20. Phase-averaged flow field with blades at  $\Psi_A=330^\circ$  and  $\Psi_B=150^\circ$  ( $\mu=0.52$ ).**



(a) Instantaneous flow visualization.

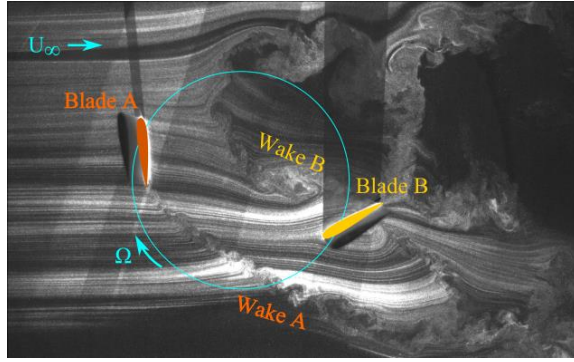


(b) Velocity field.

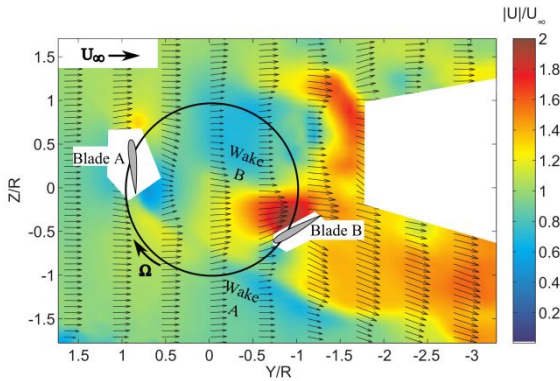


(c) Vorticity field.

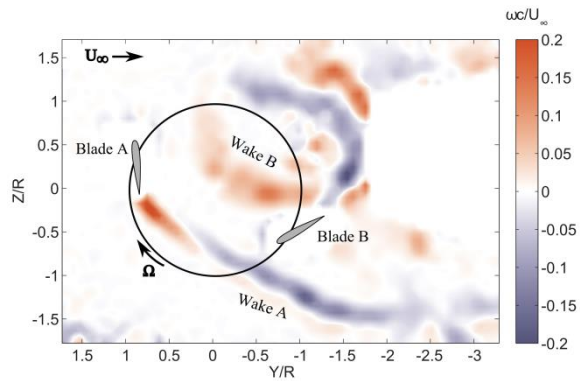
**Figure 21. Phase averaged flow field with blades at  $\Psi_A=0^\circ$  and  $\Psi_B=180^\circ$  ( $\mu=0.52$ ).**



(a) Instantaneous flow visualization.

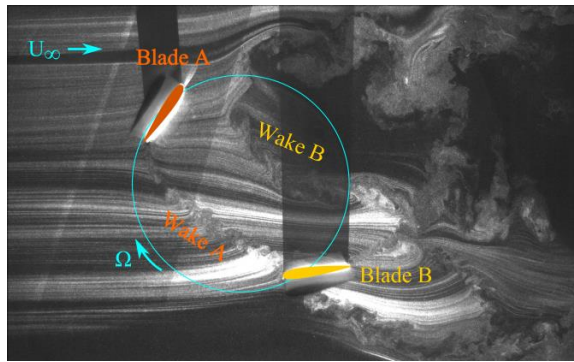


(b) Velocity field.

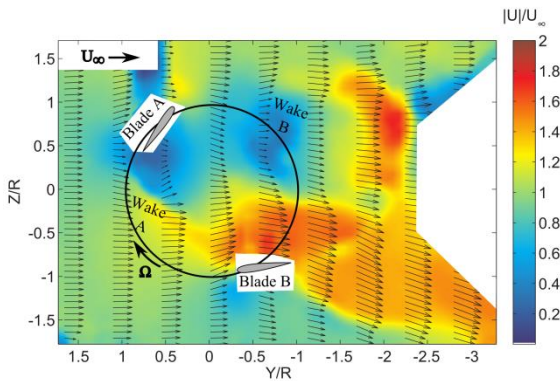


(c) Vorticity field.

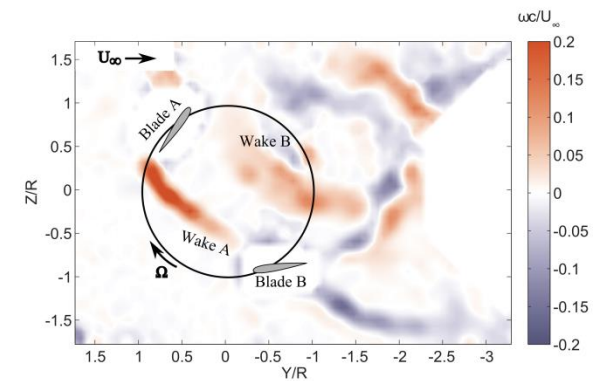
**Figure 22. Phase-averaged flow field with blades at  $\Psi_A=30^\circ$  and  $\Psi_B=210^\circ$  ( $\mu=0.52$ ).**



(a) Instantaneous flow visualization.



(b) Velocity field.



(c) Vorticity field.

**Figure 23. Phase-averaged flow field with blades at  $\Psi_A=60^\circ$  and  $\Psi_B=240^\circ$  ( $\mu=0.52$ ).**

up of small-scale vortices, a result of a Kelvin-Helmholtz instability along each shear layer (Ref. 24). The rotation direction of these vortices will become important when evaluating the blade-wake interactions that take place as blade B progresses further along the azimuth.

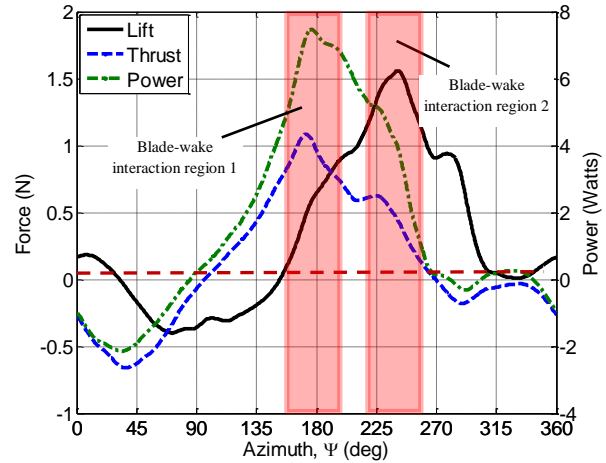
Figure 21 shows blades A and B advanced to azimuthal positions of  $\Psi_A=0^\circ$  and  $\Psi_B=180^\circ$ . The flow visualization image (Fig. 21(a)) shows the leading edge of blade B approaching the trail of counter-clockwise vortices of wake B. The velocity contour plot in Fig. 21(b) reveals a slightly increased velocity region near the upper surface of blade B.

Figure 22 shows blades A and B advanced to  $\Psi_A=30^\circ$  and  $\Psi_B=210^\circ$ . Here, a blade-wake interaction between the upper surface of blade B and the counter-clockwise vortices of wake B is evident. The velocity contours (Fig. 22(b)) show that this interaction acts to accelerate the flow over the upper surface of blade B. It was shown in the previous section that the blade operates with a positive effective angle attack and experiences high dynamic pressure in this region. These two characteristics, combined with the blade-wake interaction act to accelerate the local flow velocity on the upper surface of blade B to almost twice the freestream value. Meanwhile, the flow near blade A is nearly perpendicular to the blade chord. The flow downstream of blade A is slowed (to the right and down of the blade in Figure 22(b)); blade A is operating in a power extraction region as discussed in the previous section. This prompts a change in the direction of vorticity in the shear layer formed in wake A, as evidenced by Fig. 22(c).

Figure 23 shows the blades at  $\Psi_A=60^\circ$  and  $\Psi_B=240^\circ$ . The flow visualization image shows a second blade-wake interaction, this time between blade B and the wake of blade A, resulting in a high velocity region on the upper surface of blade B (Fig. 23(b)). This region is slower than the high velocity region associated with the first blade-wake interaction. Analysis at higher blade azimuth resolution would allow for more detailed description of the evolution of each blade-wake interaction and is a topic for further study.

It should be noted that the location and intensity of the vortices along the wakes vary with each rotor revolution due to the inherent aperiodicity of the flow. As a result, the exact position of the blade-wake interactions observed in Fig. 22-23 may vary slightly between revolutions.

Ultimately, it is important to consider the impact of these blade-wake interactions on the aerodynamic performance of the blades. The observations made from Figs. 20-23 can be used in conjunction with the CFD-predicted instantaneous lift, propulsive force, and power along the rotor azimuth to quantify the influence of the blade-wake interactions on the



**Figure 24. CFD-predicted lift, thrust and power versus azimuth at advance ratio 0.52. Regions of experimentally observed blade-wake interactions are highlighted in red.**

aerodynamic performance of the individual blades. The CFD-predicted instantaneous forces and power are presented for an advance ratio of 0.52 in Fig. 24. The regions of the experimentally observed blade-wake interactions are highlighted in red. The maximum propulsive thrust generated by the blade occurs near the first blade-wake interaction. Similarly, the maximum blade lift occurs at an azimuthal location where the second blade-wake interaction was observed. An exact one-to-one comparison of the azimuthal locations between the CFD and PIV results may not be possible here due to the unsteady nature of the flow, resolution of the image acquisition, and variation from ideal blade pitching kinematics. However, these findings collectively suggest that unsteady aerodynamic flow features and constructive blade-wake interactions in the rear half of the cyclorotor may be fundamental to enhancing the lift and propulsive thrust.

## CONCLUSIONS

The purpose of the present work was to develop a fundamental understanding of the flow physics for a MAV-scale cyclorotor in forward flight using experimental (time-resolved planar PIV and time-averaged force measurements) and computational tools (2D-CFD). In the first half of the paper, time-averaged flow field results calculated using PIV measurements were examined for different advance ratios. An aerodynamic analysis of the blades at various azimuthal locations was presented to describe the flow physics that govern the lift and propulsive force production of the cyclorotor. The second half of the paper focused on the role of unsteady aerodynamic flow features and their impact on the instantaneous force production of the blades as they travel around the rotor azimuth. The unsteady flow features were evaluated using

phase-averaged flow field measurements, with the blades at selected azimuthal locations. Observations from this analysis were correlated to CFD-predicted instantaneous aerodynamic forces and power to understand the role of blade-wake interactions in the generation of lift and propulsive force by a cyclorotor.

The key conclusions from this study can be summarized as follows:

1. The flow velocity decreases in magnitude as it passes across the upper-frontal quadrant ( $\Psi=0^\circ$  to  $\Psi=90^\circ$ ) of the cyclorotor. This is attributed to power extraction by the blades in this region. The effect of increasing advance ratio is to increase power extraction in the frontal half.
2. The primary force producing region of the cyclorotor lies in the lower-aft region of the rotor azimuth ( $\Psi=180^\circ$  to  $\Psi=270^\circ$ ). An aerodynamic analysis based on PIV time-averaged flow field measurements revealed the blades operate in a high dynamic pressure environment with a high effective angle of attack. The significant momentum addition by the blades in this region results in high flow velocity across the lower half of the rotor cage.
3. Constructive blade-wake interactions appear to play an important role in enhancing the lift and propulsive force generation of the blades in the rear half of the rotor azimuth between  $\Psi=150^\circ$  and  $\Psi=270^\circ$ . Specifically, the downstream blade encounters two blade-wake interactions: one with its own wake and another with the wake of the upstream blade. The rotational flow induced by the vortices located along the blade wakes accelerates the flow over the upper surface of the blade.

## ACKNOWLEDGEMENTS

This research was supported by the Army's MAST CTA Center for Microsystem Mechanics with Dr. Brett Piekarski (Army Research Lab) and Mr. Chris Kroninger (Army Research Lab – Vehicle Technology Directorate) as Technical Monitors. Authors would like to thank Professor Allen Winkelmann for providing use of the wind tunnel facilities at the University of Maryland.

## REFERENCES

- <sup>1</sup>Pines, D., and Bohorquez, F., "Challenges Facing Future Micro-Air-Vehicle Development," *Journal of Aircraft*, Vol. 43 (2), March/April 2006, pp. 290-305.
- <sup>2</sup>Chopra, I., "Hovering Micro Air Vehicles: Challenges and Opportunities," Proceedings of American Helicopter Society Specialists' Conference, International Forum on Rotorcraft Multidisciplinary Technology, October 15-17, 2007, Seoul, Korea.
- <sup>3</sup>Benedict, M., Jarugumilli, T., and Chopra, I., "Experimental Investigation of the Effect of Rotor Geometry and Blade Kinematics on the Performance of a MAV-Scale Cycloidal Rotor," Proceedings of the American Helicopter Society Specialists' Meeting on Unmanned Rotorcraft and Network Centric Operations, Tempe, AZ, January 25-27, 2011.
- <sup>4</sup>Benedict, M., Jarugumilli, T., Lakshminarayan, V., K., and Chopra, I., "Experimental and Computational Studies to Understand the Role of Flow Curvature Effects on the Aerodynamic Performance of a MAV-Scale Cycloidal Rotor in Forward Flight," Proceedings of the 53rd AIAA/ASME/ASCE/AHS/ASC Structures, Structural Dynamics, and Materials Conference, Honolulu, Hawaii, April 23-26, 2012.
- <sup>5</sup>Jarugumilli, T., Benedict, M., and Chopra, I., "Experimental Investigation of the Forward Flight Performance of a MAV-scale Cycloidal Rotor," Proceedings of the 68<sup>th</sup> Annual Forum of the American Helicopter Society, Fort Worth, TX, May 1-3, 2012.
- <sup>6</sup>Kirsten, F. K., "Cycloidal Propulsion Applied to Aircraft," *Transactions of the American Society of Mechanical Engineers*, Vol. 50, No. AER-50-12, 1928, pp 25-47.
- <sup>7</sup>Wheatley, J. B. and Windler, R., "Wind-Tunnel Tests of a Cyclogiro Rotor," NACA Technical Notes No. 528, May 1935.
- <sup>8</sup>Eastman, F., Cottas, N., Barkheines, G., "Wind Tunnel Tests on a High Pitch Cyclogyro," University of Washington Aeronautical Laboratory Report 191-A, 1943.
- <sup>9</sup>Nagler, B., "Improvements in Flying Machines Employing Rotating Wing Systems," United Kingdom Patent No. 280,849, issued Nov. 1926.
- <sup>10</sup>Yun, C. Y., Park, I. K., Lee, H. Y., Jung, J. S., Hwang, I. S., and Kim, S. J., "Design of a New Unmanned Aerial Vehicle Cyclocopter," *Journal of American Helicopter Society*, Vol. 52, (1), January 2007, pp. 24-35.

- <sup>11</sup>Hwang, I. S., Hwang, C. P., Min, S. Y., Jeong, I. O., Lee, C. H., Lee, Y. H. and Kim, S. J., “Design and Testing of VTOL UAV Cyclocopter with 4 Rotors,” Proceedings of the 62nd Annual Forum of the American Helicopter Society, Phoenix, AZ, April 29-May 1, 2006.
- <sup>12</sup>Iosilevskii, G., and Levy, Y., “Experimental and Numerical Study of Cyclogiro Aerodynamics,” *AIAA Journal*, Vol. 44, (12), 2006, pp 2866–2870.
- <sup>13</sup>Benedict, M., “Fundamental Understanding of the Cycloidal-Rotor Concept for Micro Air Vehicle Applications” Ph.D. Thesis, University of Maryland, College Park, MD December 2010.
- <sup>14</sup>Lakshminarayan, V. K., “Computational Investigation of Micro-Scale Coaxial Rotor Aerodynamics in Hover,” Ph.D. dissertation, Department of Aerospace Engineering, University of Maryland at College Park, 2009.
- <sup>15</sup>Pulliam, T., and Chaussee, D., “A Diagonal Form of an Implicit Approximate Factorization Algorithm,” *Journal of Computational Physics*, Vol. 39, (2), February 1981, pp. 347–363.
- <sup>16</sup>Van Leer B., “Towards the Ultimate Conservative Difference Scheme V. A Second-Order Sequel To Godunovs Method,” *Journal of Computational Physics*, Vol. 135, No. 2, 1997, pp. 229-248.
- <sup>17</sup>Roe, P., “Approximate Riemann Solvers, Parameter Vectors and Difference Schemes,” *Journal of Computational Physics*, Vol. 135, No. 2, 1997, pp. 250-258.
- <sup>18</sup>Koren, B., “Multigrid and Defect Correction for the Steady Navier-Stokes Equations”, Proceedings of the 11th International Conference on Numerical Methods in Fluid Dynamics , Williamsburg, VA, June 1988.
- <sup>19</sup>Turkel, E., “Preconditioning Techniques in Computational Fluid Dynamics,” *Annual Review of Fluid Mechanics*, Vol. 31, 1999, pp. 385–416
- <sup>20</sup>Spalart, P. R., and Allmaras, S. R., “A One-equation Turbulence Model for Aerodynamic Flows,” AIAA Paper 1992-0439, 30th AIAA Aerospace Sciences Meeting and Exhibit, Reno, NV, January 6–9, 1992.
- <sup>21</sup>Lee, Y., “On Overset Grids Connectivity and Automated Vortex Tracking in Rotorcraft CFD,” Ph.D. Dissertation, Department of Aerospace Engineering, University of Maryland at College Park, 2008.
- <sup>22</sup>Migliore, P.G., Wolfe, W.P., and Fanuccif, J.B., “Flow Curvature Effects on Darrieus Turbine Blade Aerodynamics,” *Journal of Energy*, Vol. 4, (2), 1980, pp. 49-55.
- <sup>23</sup>Jarugumilli, T., Benedict, M., and Chopra, I., “Performance and Flow Visualization Studies to Examine the Role of Pitching Kinematics on MAV-scale Cycloidal Rotor Performance in Forward Flight,” Presented at the AHS International Specialist’s Meeting on Unmanned Rotorcraft, Scottsdale, AZ, January 22-24, 2013.
- <sup>24</sup>White, F. M., *Viscous Fluid Flow*. 3<sup>rd</sup> ed. McGraw-Hill International Edition, 2006.